

Geometry-induced memory effects in isolated quantum systems: Observations and applications

Chen-Yen Lai and Chih-Chun Chien

School of Natural Sciences, University of California, Merced, CA 95343, USA.

(Dated: November 2, 2015)

Memory effects can lead to history-dependent behavior of a system, and they are ubiquitous in our daily life and have broad applications. Here we explore possibilities of generating memory effects in simple isolated quantum systems. By utilizing geometrical effects from a class of lattices supporting flat-bands consisting of localized states, memory effects could be observed in ultracold atoms in optical lattices. As the optical lattice continuously transforms from a triangular lattice into a kagome lattice with a flat band, history-dependent density distributions manifest quantum memory effects even in noninteracting systems, including fermionic as well as bosonic systems in the proper ranges of temperatures. Rapid growth in ultracold technology predicts a bright future for quantum memory-effect systems, and here two prototypical applications of geometry-induced quantum memory effects are proposed: An accelerometer recording the mechanical change rate in a coupled system and a rate-controlled memvalve where the rate of ramping the lattice potential acts as a control of the remnant density in the lattice.

PACS numbers: 67.85.-d 71.10.Ca 03.75.Kk

I. INTRODUCTION

Memory effects are ubiquitous in our daily life, ranging from the hysteresis loop in magnetization^{1,2} to rechargeable batteries^{3,4}. While the former is useful in information technology⁵, the latter limits the life of portable electronic devices. When a system exhibits memory effects, its states are history-dependent. Shape-memory materials^{6,7} and memory circuit elements^{8,9} have been explored and shown potential applications. Moreover, in artificial spin-ice reproducible microstates driven by an cyclic external field have been observed in both experiments and simulations¹⁰. Most applications and understandings of memory effects are based on classical physics, and how memory effects can arise in simple microscopic quantum systems will be the main subject investigated here.

Band theory of electrons^{5,11} based on a noninteracting picture leads to great success in modern electronics industry. Here we ask similar questions on whether noninteracting quantum systems can exhibit memory effects and what applications are out there. At first look it is counter-intuitive to consider memory effects in noninteracting systems because of a lack of competing time scales and information storage mechanism. This assertion is supported by previous work on transport in noninteracting quantum systems^{12,13} which suggests that no signature of memory effects can be observed in the steady-state current as the system is driven with different time scales.

A mathematical construction, based on the idea of a bound state that can jump into and out of a continuum in a quantum-dot system, suggests that memory effects may exist in noninteracting quantum systems¹³, although how such a system can be realized remains unclear. On the other hand, the tunability of ultracold atom experiments has allowed explorations of quantum effects in both bosonic and fermionic systems in and out of equilibrium¹⁴⁻¹⁶. While electrons are always accompanied by Coulomb interactions, interactions of cold-atoms are from two-body scattering can be turned off by applying an external magnetic field. Thus noninteracting quantum systems

are readily available¹⁷ making cold-atom systems particular suitable for unambiguous demonstrations of memory effects with or without self-interactions. Indeed, atomic superfluids exhibit hysteresis loops similar to the magnetization¹⁸ so there is no doubt memory effects can be demonstrated using cold atoms. The next milestone would be a demonstration of memory effects in noninteracting quantum systems.

Memory effects are closely tied to the dynamics and transport of the underlying systems because different evolution scenarios are needed to reveal the history of the system. Several transport phenomena in mesoscopic systems have been demonstrated in cold-atom systems¹⁹, including quantum ratchet²⁰, relaxation of fermions in optical lattice²¹, and sloshing motions²². Beside analogous phenomena in solid-state systems, cold-atom experiments can further explore spin-imbalanced fermions^{23,24}, inhomogeneous interactions²⁵⁻²⁸, and dynamical transformations of lattice geometry^{29,30}. The optical kagome lattice realized in Ref. [29] supports a flat band, which consists of localized states lacking kinetic energy. Interesting properties of flat-band systems with implications for cold atoms have been intensely studied³¹⁻³³, and the presence of a flat band can interfere with quantum transport of other mobile particles³⁴.

Here, a mechanism of memory effects based on geometrical transformations of a quantum system is analyzed, where the presence of a flat band plays an important role. The main idea is to continuously transform a system without any flat band into one with at least one flat band. As demonstrated in Ref. [29], transforming a triangular lattice into a kagome lattice has been an available technology. As the time scale of the transformation changes, evidence of memory effects showing different stationary particle distributions will be presented. To verify the contribution from the flat band, we consider another transformation from a triangular lattice to a square one, where none of the geometry supports a flat band, and show that no memory effect can be observed. In contrast to the bound state mechanism in a quantum dot discussed in Ref. [13], the flat-band mechanism finds immediate applications in cold-atom systems and is readily verifiable. Moreover, our results sug-

gest that the flat-band induced memory effect should be observable in both fermionic and bosonic systems, which will allow for broader applications.

Realizations of memory effects in simple quantum systems will allow the use of time as an additional control parameter. The hysteresis of atomic superfluid currents¹⁸ provides an example where the reversal of the current lags behind the stirring. When compared to typical electronic systems with high Fermi velocity ($\approx 10^6$ m/s) and short tunneling time (≈ 1 fs)¹¹, the relatively slow motion of cold atoms with typical tunneling time scales of ≈ 1 ms³⁵ makes them particularly suitable for unveiling mechanisms responsible for memory effects and explore their applications. For instance, an accelerometer and a density valve will be proposed here. Similar ideas can lead to novel quantum devices in atomtronics^{36,37}, where cold atoms in artificial confining potentials are employed to simulate or complement electronic devices.

This paper is organized as follows. In Sec. II, we model feasible experimental setups for lattice transformations capable of demonstrating memory effects and show a proof-of-principle demonstration that memory effects already exist in noninteracting quantum systems in the thermodynamic limit. In Sec. III, we consider real experimental conditions and simulate lattice transformations in finite size systems which model experiments more faithfully. Clear demonstrations of geometry-induced memory effects are observable in finite-size systems. Sec. IV presents two possible applications of quantum memory effects, and Sec. V concludes our study.

II. DYNAMICS AND MEMORY EFFECTS AFTER LATTICE TRANSFORMATIONS

The Hamiltonian for a two-dimensional noninteracting system in a time-dependent lattice potential is

$$\mathcal{H}(t) = -\frac{\hbar^2}{2m}\nabla^2 + V(x, y, t) = K + V. \quad (1)$$

Following Ref. [29], we consider $V(x, y, t) = V_0 [V_{tri}(x, y) + Z\gamma(t, t_r)V_{ramp}(x, y)]$, where V_0 indicates the lattice depth and $V_{tri}(x, y)$ forms a time-independent triangular lattice with lattice constant a_L . The additional potential energy, V_{ramp} , tunes the lattice to a different geometry dynamically. Here, the ramping time is t_r , Z specifies the final relative strength between V_{tri} and V_{ramp} , and $0 = \gamma(t \leq 0, t_r) \leq \gamma(t, t_r) \leq \gamma(t \geq t_r, t_r) = 1$ characterizes the ramp.

Figure 1 shows the triangular lattice with an enlarged unit cell (consisting of site- A , B , C , and D) and illustrates a transformation into the kagome lattice with $V_{ramp} = V_{ramp}^{(k)}$ and one into a square lattice with $V_{ramp} = V_{ramp}^{(s)}$. The most important difference among the triangular, square, and kagome lattices pertaining to this work is that the kagome lattice supports a flat band as summarized in Appendix A 1. Since the particles in the flat band have no kinetic energy and do not participate in transport, they introduce a different time scale from the tunneling time of mobile particles and make memory effects possible.

A. Band theory analysis

To clearly demonstrate that the flat band indeed gives rise to memory effects, we first consider the lattice transformation problem in the thermodynamic limit and implement the tight-binding approximation. The Hamiltonian in second quantized form is approximated by

$$\mathcal{H}_{tb} = \sum_{\langle ij \rangle} \Psi_i^\dagger h_{ij} \Psi_j, \quad (2)$$

where $\Psi_i^\dagger = (c_{A,i}^\dagger, c_{B,i}^\dagger, c_{C,i}^\dagger, c_{D,i}^\dagger)$ denotes the creation operator on the sites shown in Fig. 1 and h_{ij} only has finite tunneling coefficients $-\bar{t}$ along the links in the lattice. The lattice Fourier transformation, $\Psi(\mathbf{k}) = \sum_{\mathbf{r}_j} \Psi_j e^{i\mathbf{k}\cdot\mathbf{r}_j}$ leads to $\mathcal{H}_{tb} = \sum_{\mathbf{k}} \Psi^\dagger(\mathbf{k}) h(\mathbf{k}) \Psi(\mathbf{k})$ with $h_{pq} = 0$ if $p = q$ and $h_{pq} = -2\bar{t} \cos(\mathbf{k} \cdot \mathbf{a}_{pq})$ if $p \neq q$, where $p, q = A, B, C, D$ on the enlarged unit cell. The vectors \mathbf{a}_{pq} link adjacent sites p and q as shown in Fig. 1. The unitary transformation, $c_p(\mathbf{k}) = \sum_{\beta} (U)_{p\beta} c_{\beta}(\mathbf{k})$, diagonalizes the above matrix and leads to $\mathcal{H}_{tb}(\mathbf{k}) = \sum_{\beta, \mathbf{k}} E_{\beta}(\mathbf{k}) c_{\beta}^{\dagger}(\mathbf{k}) c_{\beta}(\mathbf{k})$, where $\beta = 1, 2, 3, 4$ labels the bands.

The lattice transformations are then modeled by introducing time-dependent elements of $h(\mathbf{k})$ that continuously transformed the triangular lattice to either the kagome or square lattice. The details of modeling are summarized in Appendix A 1. The interpolations between those different lattices are not unique, and here we implement a set of smooth transformations which reasonably model realistic situations. The interpolation we used will clearly prove the existence of memory effects in noninteracting quantum systems. Other interpolation schemes are expected to only introduce quantitative differences.

The time evolution of the system after the lattice-transformation potential is turned on can be monitored by the single-particle correlation matrix³⁵ $\mathcal{C}_{p,q}(\mathbf{k}) = \langle c_p^{\dagger}(\mathbf{k}) c_q(\mathbf{k}) \rangle$, whose equation of motion (EOM) can be derived from $i\hbar\partial_t c_q = [c_q, \mathcal{H}_{tb}]$ with the details shown in Appendix A 1. For noninteracting systems, the EOM has the same form for fermions and bosons. The spin-statistics (fermions vs. bosons) is reflected in the initial conditions determined by different distributions, which leads to different time-evolutions. The EOM for noninteracting systems is solved by the fourth-order Runge-Kutta method³⁸ with $\delta t = 10^{-2} t_0$, where the time unit in the tight-binding approximation is $t_0 = \hbar/\bar{t}$. In the following we will set $\hbar = 1$ and $k_B = 1$. The population of each band can be evaluated from $\mathcal{C}_{p,q}(\mathbf{k})$ by using $N_{\beta} = \sum_{\mathbf{k}} \langle c_{\beta}^{\dagger}(\mathbf{k}) c_{\beta}(\mathbf{k}) \rangle = \sum_{\mathbf{k}} \sum_{p,q} [U(\mathbf{k})]_{\beta p} \mathcal{C}_{p,q}(\mathbf{k}) [U^{\dagger}(\mathbf{k})]_{q\beta}$.

The results for single-component fermions will be presented first. Here, we consider a zero temperature initial condition and a transformation from the triangular to kagome lattice. In Fig. 2(a), the averaged particle density in third band is plotted as a function of time. Here the initial triangular lattice is half-filled, and we consider linear ramping. Thus $\gamma(t, t_r) = 0$ for $t < 0$ and $\gamma(t, t_r) = \Theta(t - t_r) + (t/t_r)\Theta(t_r - t)$ for $t \geq 0$ with a tunable ramping time t_r . Here $\Theta(x)$ is the Heaviside step function. A transformation to the square lattice

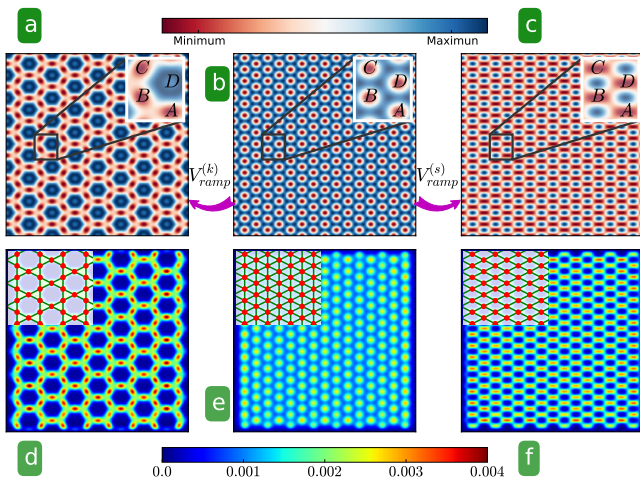


FIG. 1. (Color online) Lattice transformations from the triangular lattice (b) to the kagome lattice (a) by tuning the potential on site- D , and to the square lattice (c), where a second set of laser increases the barrier between A - D and B - C . (e)-(f) Snapshots of particle density distributions at different times from simulations: (e) Initial density distribution on the triangular lattice. The density distributions at time $t = t_0/2$ after a geometry quench to the kagome and square lattices are shown in (d) and (f) respectively. Details of the lattice structures are shown in the insets.

follows a similar protocol, and its results are summarized in Appendix. A 2.

One important feature crucial to the identification of memory effects is the emergence of a steady state as the population of each band evolves into a stationary value, which is clearly visible in Fig. 2(a). The thermal distributions in the steady states are found to deviate from the Fermi-Dirac distribution in equilibrium (shown in Appendix A 3). The existence of a steady state is nontrivial because of absence of interactions and dissipation, and the system is not expected to equilibrate. Nevertheless, for both noninteracting fermions and bosons the systems manage to evolve into steady states. Different steady-state values from different ramping times serve as clear evidence for memory effects. When ramped to a square lattice with different time scales, the final steady states reach the same density distribution on each band despite different transient behavior, as shown in Appendix A 2. Therefore, only a density re-distribution takes place but no memory effect can be observed in absence of a flat band. We have checked the lack of memory effects in transformations without a flat band for different fillings and finite temperatures, and the conclusion holds.

In stark contrast, Fig. 2(a) show that the steady-state populations in the flat band, after the triangular lattice is transformed into the kagome lattice, are different for different ramping times. This provides an unambiguous proof that geometrical effects, such as a flat band, indeed can induce memory effects in a noninteracting quantum system. The emergence of a steady state as the initial triangular lattice is transformed into the kagome lattice is highly non-trivial given

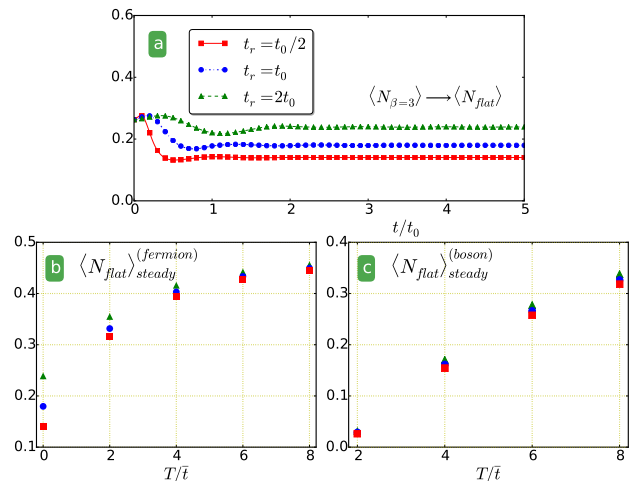


FIG. 2. (Color online) (a) Averaged fermion density on the third band, $\langle N_{\beta=3} \rangle$, after a transformation to the kagome lattice at zero temperature. Different symbols stand for different ramping times. The initial filling fraction is set to half-filling. When the kagome lattice has been reached, $t > t_r$, the third band becomes a flat band. (b) Averaged fermion density in a steady state in the kagome flat band when single component fermions undergo lattice transformations at different temperatures and ramping times. (c) The same process as (b) for noninteracting bosons.

the fact that, in density-driven transport, the flat band of the kagome lattice can interfere with the emergence of a quasi-steady state³⁵. Moreover, the longer the ramping time is chosen, the higher the population in the flat band can be observed.

Since the main contribution to the geometry-induced memory effect is from filling or emptying the flat band after a lattice transformation, an optimal condition would be that the initial population of the would-be flat band is substantially different from the populations of bands beneath or above it. Moving into or out of the flat band after a lattice transformation then causes memory effects. The flat band in the kagome lattice corresponds to the third band in the initial triangular lattice when an enlarged cell containing site- A to D is considered. Thus, prominent memory effects can be observed if the initial filling of the triangular lattice ranges from $1/2$ to $3/4$ with the detail shown in Appendix A 4. Similarly, the initial temperature can affect the initial particle distribution and influence memory effects. As the initial temperature increases, all bands tend to have more uniform distributions and memory effects are washed out. Finite-temperature effects from different initial conditions are summarized in Fig. 2(b) showing that memory effect wanes as the initial temperature increases.

B. Non-Interacting Boson

According to the results of fermions, memory effects due to the flat band is more prominent when the population in the would-be flat band is significantly different from those in nearby bands. When a Bose-Einstein condensate (BEC) exists

in the ground state, the lowest energy band is macroscopically occupied. As a consequence, higher-energy bands including the would-be flat-band have little influence so memory effects are not observable. However, noninteracting BEC cannot survive at finite temperatures in 2D and the bosons start populating all bands, so flat-band induced memory effects become more observable as temperature increases. Fig. 2(c) shows that memory effect starts to emerge in noninteracting bosons at intermediate temperatures. As temperature gets higher, bosons spread more into higher-energy bands so memory effects associated with the flat band is more prominent. However, at higher temperatures both bosons and fermions approach the classical distribution. Therefore, above quantum-degeneracy temperature there is no significant population change after lattice transformations, so memory effects vanish in the high-temperature limit.

III. FINITE SIZE SYSTEM

Cold-atom experiments are performed on finite systems and direct evaluations of their properties are highly desirable. Here we model finite systems more faithfully in real space using a finite difference method^{39,40}. Explicitly, we discretize Eq. (1) on a grid with square elements of linear size $\Delta = a_L/n_G$, where n_G is the number of grid points. We present the results with system size $(L_x, L_y) = (8\sqrt{3}, 16)a_L$ approximately corresponding to a lattice of $N_{lattice} = 16 \times 16$ sites with $n_G = 20$. Details of our approach, finite size effect, the choice of n_G , and details of ramping potentials are provided in Appendix B.

A. Single Component Fermion

For a finite-size system of noninteracting fermions, we monitor the wavefunction of an initial $T=0$ ground state. Explicitly, the energy spectrum of the triangular lattice Hamiltonian $\mathcal{H} = K + V_{tri}$ can be obtained, and by systematically estimating the number of states N_f according to the filling fraction and system size, we choose the lowest N_f states to form a Fermi sea. Next we numerically integrate the time-dependent Schrödinger equation of each eigenstate, $i\hbar\partial_t\Psi_\eta(x, y, t) = \mathcal{H}(t)\Psi_\eta(x, y, t)$, by using the fourth-order Runge-Kutta³⁸ method with a time step $\delta t = 10^{-3}t_0$. In the finite system, the unit time is $t_0 = \hbar/E_R$ with the recoil energy $E_R = \frac{\pi^2\hbar^2}{2ma_L^2}$. The evolution of the particle density can be monitored by $n(x, y, t) = \sum_{\eta=1}^N |\Psi_\eta(x, y, t)|^2$. In Fig. 1(d)-(f), the particle density contours at different times are shown for the transformations into the square and kagome lattices with a sudden quench, $\gamma(t, t_r) = \Theta(t)$. Initially, particles fill the local minima of triangular lattice potential in Fig. 1(e). After a transformation into the kagome or square lattice, particles redistribute accordingly, as shown in Fig. 1(d) and (f). Since there is no dissipation mechanism in an isolated noninteracting system, particles do not reach thermal equilibrium.

To better characterize the dynamics of lattice transforma-

tions, we define the averaged particle density at site- $\alpha \in \{A, B, C, D\}$ by

$$\langle N_\alpha(t) \rangle = \frac{\sum_{(x,y) \in \alpha} n(x, y, t)}{N_{lattice}} = \frac{N_\alpha}{N_{lattice}}. \quad (3)$$

The denominator is the total lattice points and the numerator is the summation of the particle density when its coordinate (x, y) is within a range of the corresponding lattice potential minimum. The choice of the range does not affect the result qualitatively. We monitor the particle distributions after the transformations into the square and kagome lattices. Importantly, the non-equilibrium steady states in the thermodynamic limit after lattice transformations manifest themselves here in finite-size systems, as shown in Fig. 3. In the long-time limit, the mass current decays to zero, while the particle density on each site approaches its asymptotic value. Similar to the cases in tight-binding approximation in the thermodynamic limit, the emergence of quasi steady states in finite systems is crucial because by comparing those states after lattice transformations with different time scales, memory effects can be identified.

As shown in Fig. 3(d), all quasi-steady state currents decay to zero and exhibit no memory effect. As summarized in Refs. 13 and 41, the current unavoidably misses signatures of memory effects in most cases, and our results align with this observation. Instead, we investigate the quasi-steady state particle densities and unambiguously identify memory effects associated with lattice transformations where a flat band emerges. Here the particle density is chosen close to half-filled in the initial triangular lattice. For a transformation into the square lattice, the averaged particle densities are shown in the insets of Fig. 3(a)-(c) and exhibit no memory effect.

The averaged particle densities after a transformations into the kagome lattice with different time scales, as shown in Fig. 3(a)-(c), approach different quasi-steady state values and clearly exhibit memory effects. In particular, Fig. 3(c) shows that the residue particle density on site- D highly depends on ramping time scale. For linear ramping of the lattice transformation potential, the residual density on site- D varies from less than 0.2% for $t_r = 2t_0$ to nearly 2% for the quench case ($\gamma(t, t_r) = \Theta(t)$). shown in Fig. 3(c). Since the density profiles are readily measurable in cold atoms loaded in optical lattices⁴², memory effects from the flat-band can be unambiguously observed. A measurement of the population in the flat-band of kagome lattice may also be performed by using radio-frequency spectroscopy^{43,44}.

Similar to the band analysis in the thermodynamic limit, flat-band induced memory effects are most significant when the would-be flat band has a different population from its nearby bands. To quantify the geometry-induced memory effect, we exploit the formation of quasi-steady states after lattice transformations. Explicitly, we define and evaluate the post transient time-average of the particle density on site- D as

$$\langle N_D \rangle_{steady} = \frac{\sum_{t=T_i}^{T_f} \delta t \langle N_D(t) \rangle}{T_f - T_i}. \quad (4)$$

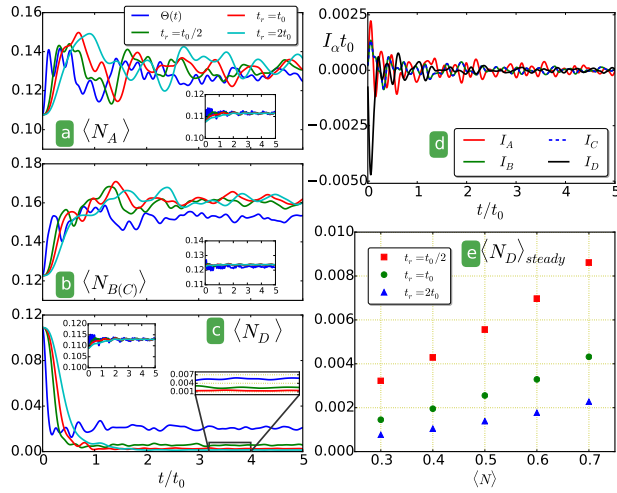


FIG. 3. (Color online) (a)-(c) Averaged density on each site versus time for single component fermions experiencing lattice transformations from the triangular to kagome lattices. The insets of (a)-(c) show the same plots for transformations from the triangular to square lattices. The quench cases are in black and the linear ramping cases with different ramping times are $t_r = t_0/2$ (red), $t_r = t_0$ (green), and $t_r = 2t_0$ (blue). (d) Averaged current, $I_\alpha = \partial_t \langle N_\alpha(t) \rangle$, for the quench case. (e) Averaged density, $\langle N_D \rangle_{steady}$, with different ramping times versus the initial filling fraction, $\langle N \rangle$. Slight differences in the initial densities on different sites are due to boundary effects discussed in Appendix B.

Here we chose $T_f = 5t_0$ and $T_i = 3t_0$, and there is no significant difference from other choices since the system has reached a quasi-steady state. For a selected initial filling, we interpret the difference between residual particles on site- D in the quasi-steady states from different ramping times as strength of memory effect and show the result in Fig. 3(e). Here we use a linear ramping function with different ramping time t_r . The difference in $\langle N_D \rangle_{steady}$ due to different ramping times increases as the filling fraction increases, which indicates stronger memory effect.

B. Condensate dynamics of weakly-interacting bosons

In contrast to fermions, single-species bosons can self interact. The Gross-Pitaevskii (GP) equation provides a suitable description of the condensate of weakly-interacting bosons far below its BEC transition temperature, and its generalization to time-dependent systems are straightforward^{15,16,39}. In the GP equation, the condensate is described by a wave function $\Phi(x, y, t)$ and

$$\left[-\frac{\hbar^2}{2m} \nabla^2 + V(x, y, t) + gN_b |\Phi|^2 \right] \Phi = i\hbar \partial_t \Phi, \quad (5)$$

where N_b is the number of bosons. Here we follow Ref. [45] to normalize the wavefunction, $\int dx dy |\Phi(x, y)|^2 = 1$. The coupling constant $g = 4\pi\hbar^2 a_s/m$ is determined by the two-body s -wave scattering length a_s . In the following we im-

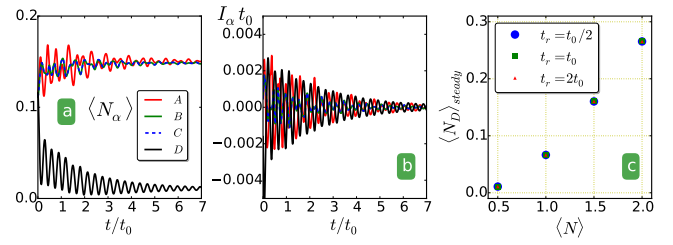


FIG. 4. (Color online) (a) Averaged density of noninteracting bosons versus time in a quench from the triangular to kagome lattices. (b) Averaged current, $I_\alpha = \partial_t \langle N_\alpha(t) \rangle$, of noninteracting bosons versus time. (c) The same plot as Fig. 3(e) for weakly-interacting bosons. Here the points collapse with each other, so no observable memory effect is present.

plement the finite-difference method to investigate condensate dynamics and set $a_s = (3/\pi)a_L$.

The particle density is given by $n(x, y, t) = N_b |\Phi(x, y, t)|^2$. In Fig. 4(a) and (b), we show the averaged density and current in each site after a quench into the kagome lattice. When compared to the fermion case, it takes a longer time for weakly-interacting bosons to reach a quasi-steady state. The emergence of a quasi steady state in interacting bosons has been studied in Ref. [46], and here quasi-steady states after different lattice transformation protocols allow us to detect memory effects.

In the presence of Bose-Einstein condensation, the lowest energy state is macroscopically occupied while other states have relatively small weight. Since there are two dispersive bands beneath the flat band in the kagome lattice, during and after the lattice transformation, the condensate is less likely to spread into higher bands even when the filling fraction is large. Observation of flat-band induced memory effects is thus unlikely in weakly interacting bosons in its condensed phase. Fig. 4(c) shows the time average of particle density on site- D . One can see that the long-time averaged densities are the same regardless of different ramping times, and there is no observable change as the initial filling increases. Stronger interaction strength has also been tested and there is no observable flat-band induced memory effect in the condensate.

We remark that memory effects due to the phase stiffness of superfluids have been observed in the hysteresis loops of bosonic atoms in a ring-shape geometry⁴⁷. The flat-band induced memory effects discussed here, although not observable in the superfluid phase due to BEC in the ground state, apply to both noninteracting bosons and fermions and complement the memory effects due to long-range orders in superfluids.

IV. APPLICATIONS

On the experiment side, the triangular, square, and kagome optical lattices have all been realized^{29,30} and loaded with bosonic atoms. Feasibility of dynamical ramping is also presented in Ref. [29]. While measurements of the population in a selected band can be challenging in solid-state materials, in

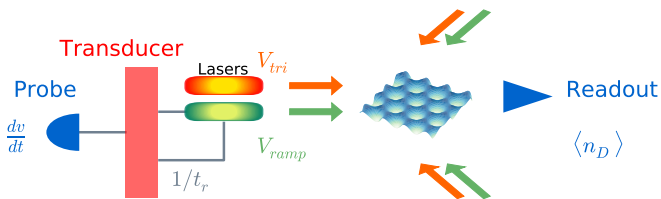


FIG. 5. (Color online) Illustration of a memory-effect accelerometer. The probe receives velocity changes as its signal, and a transducer ramps up the laser for transforming the lattice according to acceleration of the probe. The readout reveals different densities on D -site due to different accelerations.

cold-atoms real space density distributions can be mapped out by in-situ imaging⁴². Moreover, the population of a flat band can be measured by time-of-flight experiments⁴⁸. Combining those imaging techniques with capability of tuning the lattice geometry by controlling laser intensity, here we propose two applications of geometry-induced memory effects.

The first application is an accelerometer, illustrated in Fig. 5, where a probe is connected to a piezoelectric piece that controls the laser responsible for V_{ramp} . When the probe is accelerated, the change of voltage from the piezoelectric piece ramps up V_{ramp} and transforms an initially loaded triangular lattice into a kagome lattice. The remaining density on D -sites is sensitive to the rate at which V_{ramp} was switched on, hence records the acceleration in the probe. Although one may simply record signals from the transducer and numerically differentiate the signals with respect to time to extract the rate of change, lattice-transformation induced memory effects automatically record, in the remaining D -site density, the rate of the change sensed by the probe. Since memory effects in the kagome lattice are most prominent if the ramping time is about the same order of magnitude as the tunneling time, this type of accelerometers will be more efficient in probing changes in the ms-scale.

A second application is a rate-controlled memvalve, where the ramping potential V_{ramp} controlled by laser intensity is switched on at different rates to control the remaining density n_D on the D -sites of the kagome lattice. Different ramping rates then lead to different n_D , which can be read out using the above-mentioned imaging techniques. After one operation, V_{ramp} is turned off and the triangular lattice is replenished with fresh cold-atoms, and the next operation starts.

The mechanism behind the memvalve is remotely analogous to an electronic transistor⁴⁹, where a gate voltage controls the current from the source to the drain. In the memvalve, however, the control is the rate of ramping up V_{ramp} . A comparison of the memvalve and transistor is summarized in Table I. Recent experimental progress in rapid loading and manipulating cold atoms⁵⁰ and portable cold-atom technology⁵¹ could make the accelerometer and rate-controlled memvalve realistic in the near future.

Transistor		Rate-controlled Memvalve	
Control	Output	Control	Output
Voltage	Current	Rate	Density
V_1	$I_1 > I_c$	$1/t_{r1}$	$N_{D1} > N_c$
V_2	$I_2 < I_c$	$1/t_{r2}$	$N_{D2} < N_c$

TABLE I. (Color online) Comparison between electronic transistor and the proposed rate-controlled memvalve.

V. CONCLUSIONS

Memory effects are shown to exist in noninteracting quantum systems when a flat band emerges. Identification of memory effects was made possible due to emergence of non-trivial steady states after a lattice transformation. Different density distributions following different ramping times serve as direct evidence for memory effects, which are readily observable in fermionic systems at low temperatures and bosonic systems at intermediate temperatures. Since flat-bands can be found in a variety of lattice geometries, including saw-tooth⁵², cross stitch^{53,54}, photonic rhombic lattice⁵⁵, and the recently realized optical or photonic Lieb lattice⁵⁶⁻⁵⁸, geometry-induced memory effects may also be studied in those systems. On the other hand, photon-induced memory effects have been claimed in certain materials exhibiting structural transitions^{59,60}, and tunability of optical-lattice geometry can provide opportunities for bridging our understanding of memory effects in material science and ultracold atoms.

The geometry-induced quantum memory effect is less prominent in the presence of BEC, but phase-stiffness induced memory effects manifested by hysteresis of the vorticity have been observed in interacting bosons in the superfluid phase¹⁸. Given the variety of memory effects and broad range of their applications including the accelerometer and memvalve discussed here, novel quantum devices utilizing memory effects are promising in the emerging field of atomtronics^{36,37}.

ACKNOWLEDGMENTS

We thank Gia-Wei Chern, Massimiliano Di Ventra, Dan Stamper-Kurn, Michael Zwolak, and YangQuan Chen for useful discussions.

Appendix A: Band Theory and Dynamics

1. Model and Method

In the thermodynamic limit, the system is approximated by the one-band tight binding model

$$\mathcal{H}_{tb} = \sum_{\langle ij \rangle} \Psi_i^\dagger h_{ij} \Psi_j, \quad (\text{A1})$$

where $\Psi_i^\dagger = (c_{A,i}^\dagger \ c_{B,i}^\dagger \ c_{C,i}^\dagger \ c_{D,i}^\dagger)$ is the creation operators on each site. From Fig. 1, the A - B link is connected by a vector $\mathbf{a}_{AB} = (-\sqrt{3}/2, 1/2)a_L$, and the rest of the links can be determined as well. After performing the Fourier transformation $\Psi(\mathbf{k}) = \sum_{\mathbf{r}_j} \Psi_j e^{i\mathbf{k}\cdot\mathbf{r}_j}$, we are able to obtain the Hamiltonian in momentum space as $\mathcal{H}_{tb} = \sum_{\mathbf{k}} \Psi^\dagger(\mathbf{k}) h(\mathbf{k}) \Psi(\mathbf{k})$, where the elements of $h(\mathbf{k})$ are $h_{pq} = 0$ if $p = q$ and $h_{pq} = -2\bar{t} \cos(\mathbf{k} \cdot \mathbf{a}_{pq})$ if $p \neq q$ and $p, q = A, B, C, D$. During the dynamical ramping to the kagome or square lattice, $h^{(k/s)}(\mathbf{k})$ becomes time dependent. Explicitly,

$$h^{(k)}(\mathbf{k}) = \begin{pmatrix} 0 & h_{AB} & h_{AC} & h_{AD}^{(k)} \\ h_{AB} & 0 & h_{BC} & h_{BD}^{(k)} \\ h_{AC} & h_{BC} & 0 & h_{CD}^{(k)} \\ h_{AD}^{(k)} & h_{BD}^{(k)} & h_{CD}^{(k)} & h_{DD}^{(k)} \end{pmatrix}, \quad (\text{A2})$$

where $h_{pD}^{(k)}(t) = [1 - \gamma(t, t_0)] h_{pD}$ and $h_{DD}^{(k)}(t) = \gamma(t, t_0) \Delta_D$ with a final potential difference $\Delta_D = 8\bar{t}$ on site D . Although the potential energy on site- D is still finite, we assume that the hopping amplitude decays to zero when the ramping is finished. The assumption is valid following available experimental results²⁹. When ramping to the square lattice, the time-dependent Hamiltonian can be written as

$$h^{(s)}(\mathbf{k}) = \begin{pmatrix} 0 & h_{AB} & h_{AC} & h_{AD}^{(s)} \\ h_{AB} & 0 & h_{BC} & h_{BD}^{(s)} \\ h_{AC} & h_{BC} & 0 & h_{CD}^{(s)} \\ h_{AD}^{(s)} & h_{BD}^{(s)} & h_{CD}^{(s)} & 0 \end{pmatrix}, \quad (\text{A3})$$

where $h_{AD(BC)}^{(s)}(t) = [1 - \gamma(t, t_0)] h_{AD(BC)}$. Details of the lattice structures are shown in Fig. 1.

Here we focus on the case of a transformation to the kagome lattice. The Hamiltonian at each time slot is diagonalized to obtain the corresponding energy spectrum. In Fig. 6, we plot the energy spectrum at different time slots. The zone points (Γ , K , and M) are defined on the kagome Brillouin zone, which is the reason why the spectrum of the triangular lattice shown in Fig. 6(a) has four bands. As the potential energy (Δ_D) on site- D increases, the fourth band energy rises and the third band evolves into a flat band. After the ramping is completed, the lower three bands forms the kagome band structure and the highest band represents the particles on site- D as shown in Fig. 6(d).

The time evolution of the single-particle correlation ma-

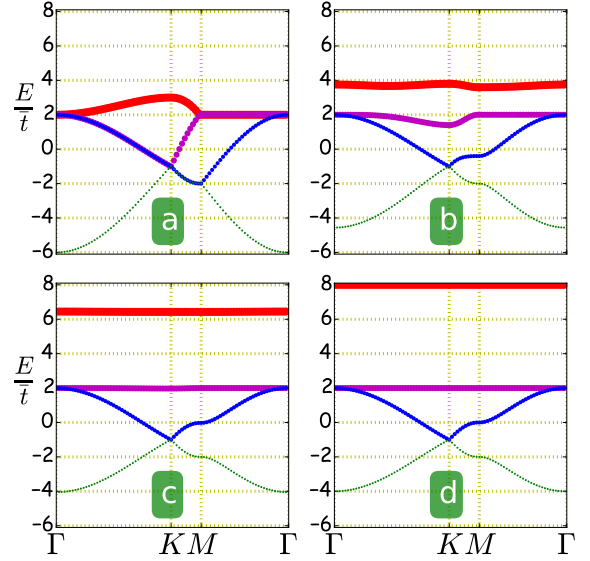


FIG. 6. (Color online) Tight-binding bands at different times in a transformation from the triangular to kagome lattice: (a) $t = 0$, (b) $t = 0.4t_0$, (c) $t = 0.8t_0$, and (d) $t = t_0$. Here the ramping function is linear with ramping time $t_r = t_0$. The third band (purple) develops into a flat band.

trix³⁵ $\mathcal{C}_{p,q}(\mathbf{k}) = \langle c_p^\dagger(\mathbf{k}) c_q(\mathbf{k}) \rangle$ is governed by

$$\begin{aligned} i \frac{\partial}{\partial t} \langle c_p^\dagger(\mathbf{k}) c_q(\mathbf{k}) \rangle & \quad (\text{A4}) \\ & = \sum_j [h_{jp}(\mathbf{k}) \langle c_j^\dagger(\mathbf{k}) c_q(\mathbf{k}) \rangle - h_{qj}(\mathbf{k}) \langle c_p^\dagger(\mathbf{k}) c_j(\mathbf{k}) \rangle], \end{aligned}$$

which applies to both fermions and bosons. The initial matrix elements should be determined by the corresponding spin-statistics at given temperature T . For single-component fermions, the filling is given by $N_{tot}/N_{lattice} = \sum_{\beta, \mathbf{k}} \langle c_\beta^\dagger(\mathbf{k}) c_\beta(\mathbf{k}) \rangle$, where N_{tot} and $N_{lattice}$ denote the total particle number and lattice number, and $\langle c_\beta^\dagger(\mathbf{k}) c_\beta(\mathbf{k}) \rangle = \{\exp((E_\beta(\mathbf{k}) - \mu)/k_B T) + 1\}^{-1}$ with μ and k_B denoting the chemical potential and Boltzmann constant. Therefore, the initial correlation matrix can be inferred from $\mathcal{C}_{p,q}(\mathbf{k}) = \sum_{\beta, \beta'} (U^\dagger)_{\beta p} \langle c_\beta^\dagger(\mathbf{k}) c_{\beta'}(\mathbf{k}) \rangle U_{q \beta'}$, where U diagonalizes the Hamiltonian at the given time.

2. Compare to Square Lattice

In Fig. 7, we show the simulation result by monitoring the dynamics of two different geometrical transformations, one to the kagome lattice and the other to the square lattice. There is no observable memory effects in the square lattice case and the averaged density on each site approaches the same steady-state value. The reason we have four bands instead of one for the triangular and square lattices is because we use the same enlarged unit cell to make a fair comparison with the

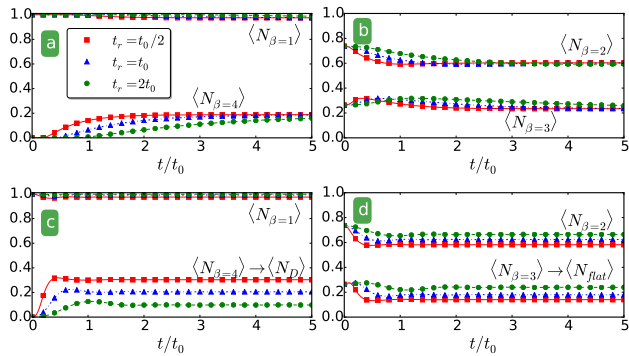


FIG. 7. (Color online) Averaged fermion density in each band versus time. (a)-(b) correspond to a transformation into the square lattice and (c)-(d) correspond to a transformation into the kagome lattice at zero temperature. The different symbols stand for different ramping times. The filling fraction is set to half-filling. In (a) and (c), the populations of the lowest ($\beta = 1$) and highest ($\beta = 4$) bands are shown. In (b) and (d), the populations of the second and third ($\beta = 2, 3$) bands are shown.

kagome lattice. On the other hand, memory effect shows up in the kagome lattice as the averaged density in each band varies with different ramping times. As we mentioned in the main text, a major difference between the square and kagome lattices is the presence of a flat band, which is the source of the memory effects observed here. We remark that the models used here does not remove the site- D from the lattice but only increased its on-site energy and set the associated hopping amplitude to zero. Hence we still have residual density on site- D as shown in Fig. 7(c) after a lattice transformation.

3. Non-Thermalized Steady States

In both finite-size and thermodynamic-limit cases, steady states in the long-time limit have been observed. In a closed system with energy conservation, we found the duration of a quasi-steady state proportional to its size. We have verified that steady states in the thermodynamic limit observed here do not correspond to any thermal state. In Fig. 8, we show three different cases, where the left column shows the initial distributions and the right shows the distributions at a later time after the lattice geometry is transformed. In the first case, the result of ramping to the square lattice is also observable. In the second cases, the initial state follows the Fermi-Dirac distribution at zero temperature. After ramping to the kagome lattice, the later state is not a well-defined thermal distribution since the density distribution depends not only on the energy but also the momentum. Similar behavior happens when the initial state is a thermalized state in the third case. In the later state one can see multi-values of the distribution although the distribution is stationary implying a steady state.

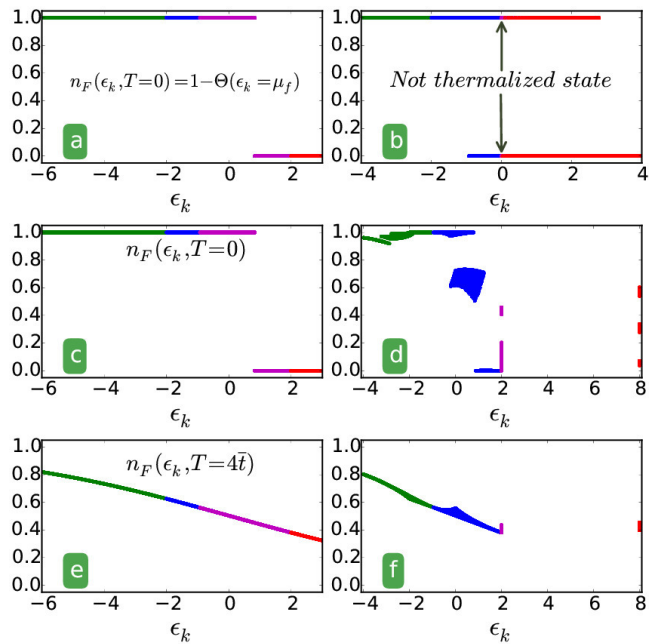


FIG. 8. (Color online) Initial $t = 0$ (left column) and later $t = 6t_0$ (right column) density distributions of fermions for three different cases: (a)-(b) correspond to a transformation to the square lattice at zero temperature. (c)-(d) correspond to a transformation to the kagome lattice at zero temperature. (d)-(e) correspond to a transformation to the kagome at $k_B T = 4\bar{t}$. The distributions on the left column are thermal distributions but those on the right are not.

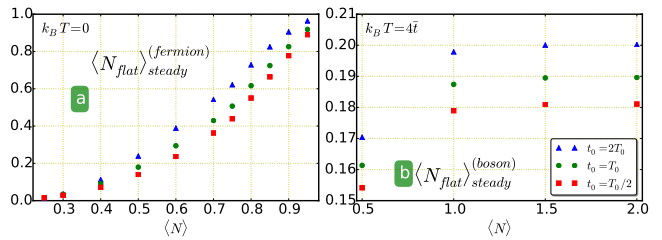


FIG. 9. (Color online) (a) Averaged fermion density in a steady state in the kagome flat band versus the initial filling. (b) The same plot for non-interacting bosons at $T = 4\bar{t}$ with $k_B = 1$.

4. Filling Dependence

One subtle difference between the band theory in the thermodynamic limit and the finite-system scheme is that in the band theory only one fermion can occupy one lattice site, while in the finite-size scheme there can be more than one orbitals in a single lattice site because we have used Δ^2 grid points to simulate one single lattice site. We mentioned that the geometry-induced memory effects are prominent if the initial filling of the triangular lattice ranges from $1/2$ to $3/4$ for fermions at zero temperature. Fig. 9 shows memory effects for single-component fermions at zero temperature and non-

interacting bosons at $T = 4\bar{t}$. For fermions, stronger memory effect can be observed around 3/4 filling since in the initial distribution, the highest band is empty and the third band is completely filled. Memory effects become weaker once the filling fraction is larger than 3/4. When all bands are completely filled, no memory effect can be observed since there is no exchange of populations in the bands. For bosons, the filling fraction can be any positive number due to the Bose statistics. In Fig. 9(b), the difference of the flat-band density following different ramping times does not increase significantly as the filling fraction gets larger than one, which suggests that memory effects of non-interacting bosons would saturate at high density.

Appendix B: Finite Difference Method and Finite Size Effect

Here we present the details of our analysis of finite systems. We use the finite-difference method^{39,40} to rewrite continuous derivatives as finite differences defined on discretized square elements of linear size Δ by choosing $\Delta = a_L/n_G$, where n_G is the number of grid points in each direction. Here we discuss finite-size effects and the dependence of our results on n_G . The Schrödinger equation governed by Hamiltonian in Eq. (1) is discretized on a two dimensional grid labeled by index $j = 0, 1, \dots, n_G$ in each direction. To be specific, we have the matrix elements (with $\hbar = m = 1$)

$$K_{j,j} = \frac{2}{\Delta^2}, \quad (\text{B1})$$

$$K_{j,j+1} = -\frac{1}{2\Delta^2} \quad (\text{B2})$$

for kinetic energy and

$$V_{jl} \approx \delta_{j,l} V(r_j), \quad (\text{B3})$$

for potential energy which is diagonal. For this method to be valid, $V(r)$ should be slowly varying against Δ . This approach is also used to discretize the Gross-Pitaevskii equation, in which a non-linear term, $gN_b|\phi|^2$, is included in the equation of motion.

The detailed potential energy for the triangular lattice is

$$\begin{aligned} & V_{tri}(x, y) \quad (\text{B4}) \\ & = \sin^2\left(\frac{\pi x}{2a_L}\right) \sin^2\left(\frac{\pi x}{2a_L} + \frac{\sqrt{3}\pi y}{2a_L}\right) + \sin^2\left(\frac{\pi x}{2a_L} - \frac{\sqrt{3}\pi y}{2a_L}\right), \end{aligned}$$

which has a minimum at the origin. For a transformation to the kagome lattice, another set of lasers focused on the minimum points of $V_{tri}(x, y)$ with twice the wavelength is used, which

may be modeled by

$$\begin{aligned} & V_{ramp}^{(k)} \quad (\text{B5}) \\ & = \sin^2\left(\frac{\pi x}{a_L}\right) + \sin^2\left(\frac{\pi x + \sqrt{3}\pi y}{a_L}\right) + \sin^2\left(\frac{\pi x - \sqrt{3}\pi y}{a_L}\right). \end{aligned}$$

Finally, to achieve the square lattice, a second set of lasers with shifted focus points and the same wavelength as $V_{tri}(x, y)$ is modeled by

$$\begin{aligned} & V_{ramp}^{(s)} = \sin^2\left(\frac{x}{2a_L}\right) \quad (\text{B6}) \\ & + \sin^2\left(\frac{x + \sqrt{3}(y - a_L/2)}{2a_L}\right) + \sin^2\left(\frac{x - \sqrt{3}(y - a_L/2)}{2a_L}\right). \end{aligned}$$

The total potential energy is $V(x, y, t) = V_0 [V_{tri}(x, y) + Z\gamma(t, t_r)V_{ramp}(x, y)]$, and we set $V_0 = 4E_R$ and $Z=6$ in this work.

Besides Fig. 3, we also compare the results with different system size and different numbers of grid points. The comparisons are shown in the top (bottom) row of Fig. 10 for different numbers of lattice sites (grid points). For a given system with $(L_x, L_y) = (8\sqrt{3}, 16)a_L$, the number of minima in each direction is $(N_x, N_y) = (L_x/(\sqrt{3}a_L/2), L_y/a_L)$ and the system has approximately $N_x \times N_y$ lattice sites. We use the above expression to label system size in Fig. 10 and compare different system size with fixed number of grid points $n_G = 20$. First, we evaluate the initial densities on the sub-lattices corresponding to the A, B, C, D-sites. Although the initial filling is the same, the density distributions on different sub-lattices are slightly different due to boundary effects because open boundary condition requires wave functions to vanish at the boundary. For instance, in a 16×16 system, site-*A* and *D* are located on the boundary, so they have relatively lower density when compared to site *B* and *C*. On the other hand, in 18×18 and 14×14 systems the densities on site-*A* and *D* are closed to each other. By considering the small offsets from the initial densities on different sites, the results from different system sizes agree qualitatively. Most importantly, the residual density on site-*D* is insensitive of system size and thus can serve as a signature of memory effect. For different numbers of grid points, we choose the system size to be 16×16 . As mentioned before, the number n_G needs to be large enough to make the above approach valid, a condition equivalent to the requirement that $V(x)$ should be slow vary against Δ . Moreover, the choice of n_G may be interpreted as the number of effective orbitals on each lattice site. A finite number of effective orbitals allows a more detailed description physics of finite-size systems and rule out a dynamically-generated insulator⁴¹.

The results with three different values n_G are shown in the bottom row of Fig. 10. The results with $n_G = 20$ and 30 agree with each other quite well. For the $n_G = 10$ case, the initial density distribution is slightly different due to boundary effects, especially on site-*B* and *C*, leading to a slightly different quasi-steady state value. Nevertheless, all cases show the same qualitative behavior.

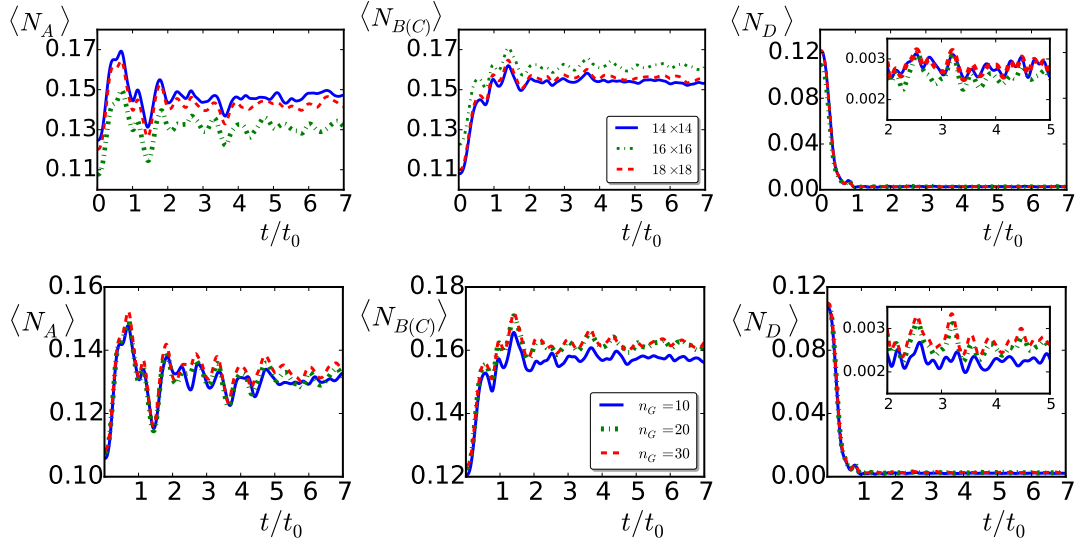


FIG. 10. (Color online) Averaged fermion density in a transformation to the kagome lattice with a linear ramping function and ramping time $t_r = t_0$. The initial filling is set to half-filling. Top row: Comparisons of different system sizes. Different colors represent different numbers of effective lattice points on the triangular lattice. Bottom row: Comparisons of different numbers of grid points (n_G).

- ¹ J. D. Jackson, *Classical electrodynamics*, 3rd ed. (John Wiley and Sons, 1999).
- ² Y. Sun, M. B. Salamon, K. Garnier, and R. S. Averback, “Memory Effects in an Interacting Magnetic Nanoparticle System,” *Phys. Rev. Lett.* **91**, 167206 (2003).
- ³ D. Liden and T. B. Reddy, *Handbook of batteries*, 3rd ed. (McGraw-Hill, 2001).
- ⁴ T. Sasaki, Y. Ukyo, and P. Novák, “Memory effect in a lithium-ion battery,” *Nature Materials* **12**, 569–575 (2013).
- ⁵ N. A. Gershenfeld, *The physics of information technology*, Vol. 25 (Cambridge University Press Cambridge, 2000).
- ⁶ M. Ebara, Y. Kotsuchibashi, R. Narain, N. Idota, Y. J. Kim, J. M. Hoffman, K. Uto, and T. Aoyagi, *Smart biomaterials* (Springer, Berlin, 2014).
- ⁷ J. Cui, “Shape memory alloys and their applications in power generation and refrigeration,” in *Mesoscope phenomena in multifunctional materials: Synthesis, characterization, modeling, and applications*, edited by A. Saxena and A. Planes (Springer-Verlag, Berlin, 2014).
- ⁸ Y. V. Pershin and M. Di Ventra, “Memory effects in complex materials and nanoscale systems,” *Adv. Phys.* **60**, 145–227 (2011).
- ⁹ R. Marani, G. Gelao, and A. G. Perri, “A review on memristor applications,” arXiv:1506.06899 (2015).
- ¹⁰ I. Gilbert, G.-W. Chern, B. Fore, Y. Lao, S. Zhang, C. Nisoli, and P. Schiffer, “Direct Visualization of Memory Effects in Artificial Spin Ice,” arXiv:1508.06330 (2015).
- ¹¹ N. W. Ashcroft and N. D. Mermin, *Solid state physics* (Saunders College, 1976).
- ¹² C. C. Chien and M. Di Ventra, “Controlling transport of ultra-cold atoms in 1d optical lattices with artificial gauge fields,” *Phys. Rev. A* **87**, 023609 (2013).
- ¹³ H. D. Cornean, A. Jensen, and G. Nenciu, “Memory Effects in Non-Interacting Mesoscopic Transport,” *Ann. Henri Poincaré* **15**, 1919–1943 (2013).
- ¹⁴ I. Bloch and W. Zwerger, “Many-body physics with ultracold gases,” *Rev. Mod. Phys.* **80**, 885–964 (2008).
- ¹⁵ C. J. Pethick and H. Smith, *Bose–Einstein Condensation in Dilute Gases*, 2nd ed. (Cambridge University Press, Cambridge, 2010).
- ¹⁶ H. T. C. Stoof, D. B. M. Dickerscheid, and K. Gubbels, *Ultracold Quantum Fields*, Theoretical and Mathematical Physics (Springer Netherlands, Dordrecht, 2008).
- ¹⁷ C. Chin, R. Grimm, P. S. Julienne, and E. Tiesinga, “Feshbach resonances in ultracold gases,” *Rev. Mod. Phys.* **82**, 1225–1286 (2010).
- ¹⁸ S. Eckel, J. G. Lee, F. Jendrzejewski, N. Murray, C. W. Clark, C. J. Lobb, W. D. Phillips, M. Edwards, and G. K. Campbell, “Hysteresis in a quantized superfluid ‘atomtronic’ circuit,” *Nature* **506**, 200–203 (2014).
- ¹⁹ C. C. Chien, S. Peotta, and M. Di Ventra, “Quantum transport in ultracold atoms,” arXiv:1504.02907 (2015).
- ²⁰ T. Salger, S. Kling, T. Hecking, C. Geckeler, L. Morales-Molina, and M. Weitz, “Directed Transport of Atoms in a Hamiltonian Quantum Ratchet,” *Science* **326**, 1241–1243 (2009).
- ²¹ U. Schneider, L. Hackermüller, J. P. Ronzheimer, S. Will, S. Braun, T. Best, I. Bloch, E. Demler, S. Mandt, D. Rasch, and A. Rosch, “Fermionic transport and out-of-equilibrium dynamics in a homogeneous Hubbard model with ultracold atoms,” *Nat Phys* **8**, 213–218 (2012).
- ²² H. Ott, E. de Mirandes, F. Ferlaino, G. Roati, G. Modugno, and M. Inguscio, “Collisionally Induced Transport in Periodic Potentials,” *Phys. Rev. Lett.* **92**, 160601 (2004).
- ²³ G. B. Partridge, W. Li, Y. A. Liao, R. Hulet, M. Haque, and H. Stoof, “Deformation of a Trapped Fermi Gas with Unequal Spin Populations,” *Phys. Rev. Lett.* **97**, 190407 (2006).
- ²⁴ M. W. Zwierlein, A. Schirotzek, C. H. Schunck, and W. Ketterle, “Fermionic Superfluidity with Imbalanced Spin Populations,” *Sci-*

- ence **311**, 492–496 (2006).
- ²⁵ T. Fukuhara, S. Sugawa, Y. Takasu, and Y. Takahashi, “All-optical formation of quantum degenerate mixtures,” *Phys. Rev. A* **79**, 021601 (2009).
 - ²⁶ R. Yamazaki, S. Taie, S. Sugawa, and Y. Takahashi, “Submicron Spatial Modulation of an Interatomic Interaction in a Bose-Einstein Condensate,” *Phys. Rev. Lett.* **105**, 050405 (2010).
 - ²⁷ S. Blatt, T. L. Nicholson, B. J. Bloom, J. R. Williams, J. W. Thomsen, P. S. Julienne, and J. Ye, “Measurement of Optical Feshbach Resonances in an Ideal Gas,” *Phys. Rev. Lett.* **107**, 073202 (2011).
 - ²⁸ H. Wu and J. E. Thomas, “Optical Control of Feshbach Resonances in Fermi Gases Using Molecular Dark States,” *Phys. Rev. Lett.* **108**, 010401 (2012).
 - ²⁹ G.-B. Jo, J. Guzman, C. K. Thomas, P. Hosur, A. Vishwanath, and D. M. Stamper-Kurn, “Ultracold Atoms in a Tunable Optical Kagome Lattice,” *Phys. Rev. Lett.* **108**, 045305 (2012).
 - ³⁰ L. Tarruell, D. Greif, T. Uehlinger, G. Jotzu, and T. Esslinger, “Creating, moving and merging Dirac points with a Fermi gas in a tunable honeycomb lattice,” *Nature* **483**, 302–305 (2012).
 - ³¹ C. Wu, D. Bergman, L. Balents, and S. Das Sarma, “Flat bands and wigner crystallization in the honeycomb optical lattice,” *Phys. Rev. Lett.* **99**, 070401 (2007).
 - ³² N. R. Cooper and J. Dalibard, “Reaching Fractional Quantum Hall States with Optical Flux Lattices,” *Phys. Rev. Lett.* **110**, 185301 (2013).
 - ³³ T. Paananen and T. Dahm, “Topological flat bands in optical checkerboardlike lattices,” *Phys. Rev. A* **91**, 033604 (2015).
 - ³⁴ G.-W. Chern, C.-C. Chien, and M. Di Ventra, “Dynamically generated flat-band phases in optical kagome lattices,” *Phys. Rev. A* **90**, 013609 (2014).
 - ³⁵ C.-C. Chien, M. Zwolak, and M. Di Ventra, “Bosonic and fermionic transport phenomena of ultracold atoms in one-dimensional optical lattices,” *Phys. Rev. A* **85**, 041601 (2012).
 - ³⁶ B. T. Seaman, M. Krämer, D. Z. Anderson, and M. J. Holland, “Atomtronics: Ultracold-atom analogs of electronic devices,” *Phys. Rev. A* **75**, 023615 (2007).
 - ³⁷ R. A. Pepino, J. Cooper, D. Z. Anderson, and M. J. Holland, “Atomtronic Circuits of Diodes and Transistors,” *Phys. Rev. Lett.* **103**, 140405 (2009).
 - ³⁸ W. H. Press, S. A. Teukolsky, W. T. Vetterling, and B. P. Flannery, *Numerical Recipes 3rd Edition: The Art of Scientific Computing*, 3rd ed. (Cambridge University Press, New York, NY, USA, 2007).
 - ³⁹ D. Vudragović, I. Vidanović, A. Balaž, P. Muruganandam, and S. K. Adhikari, “C programs for solving the time-dependent Gross–Pitaevskii equation in a fully anisotropic trap,” *Computer Physics Communications* **183**, 2021–2025 (2012).
 - ⁴⁰ W. Bao and Q. Du, “Computing the Ground State Solution of Bose–Einstein Condensates by a Normalized Gradient Flow,” *SIAM Journal on Scientific Computing* **25**, 1674–1697 (2006).
 - ⁴¹ C.-C. Chien, D. Gruss, M. Di Ventra, and M. Zwolak, “Interaction-induced conducting–non-conducting transition of ultra-cold atoms in one-dimensional optical lattices,” *New J. Phys.* **15**, 063026 (2013).
 - ⁴² N. Gemelke, X. Zhang, C.-L. Hung, and C. Chin, “In situ observation of incompressible Mott-insulating domains in ultracold atomic gases,” *Nature* **460**, 995–998 (2009).
 - ⁴³ P. Lee, M. Anderlini, B. Brown, J. Sebby-Strabley, W. Phillips, and J. Porto, “Sublattice Addressing and Spin-Dependent Motion of Atoms in a Double-Well Lattice,” *Phys. Rev. Lett.* **99**, 020402 (2007).
 - ⁴⁴ J. T. Stewart, J. P. Gaebler, and D. S. Jin, “Using photoemission spectroscopy to probe a strongly interacting Fermi gas,” *Nature* **454**, 744–747 (2008).
 - ⁴⁵ M. Cerimele, M. Chiofalo, F. Pistella, S. Succi, and M. Tosi, “Numerical solution of the Gross–Pitaevskii equation using an explicit finite-difference scheme: An application to trapped Bose-Einstein condensates,” *Phys. Rev. E* **62**, 1382–1389 (2000).
 - ⁴⁶ S. Peotta, C.-C. Chien, and M. Di Ventra, “Phase-induced transport in atomic gases: From superfluid to Mott insulator,” *Phys. Rev. A* **90**, 053615 (2014).
 - ⁴⁷ K. Henderson, C. Ryu, C. MacCormick, and M. G. Boshier, “Experimental demonstration of painting arbitrary and dynamic potentials for Bose–Einstein condensates,” *New J. Phys.* **11**, 043030 (2009).
 - ⁴⁸ S. T. Wang, D. L. Deng, and L. M. Duan, “Probe of Three-Dimensional Chiral Topological Insulators in an Optical Lattice,” *Phys. Rev. Lett.* **113**, 033002 (2014).
 - ⁴⁹ P. Horowitz and W. Hill, *The art of electronics*, 2nd ed. (Cambridge University Press, Cambridge, 1989).
 - ⁵⁰ B. J. Lester, N. Luick, A. M. Kaufman, C. M. Reynolds, and C. A. Regal, “Rapid production of uniformly-filled arrays of neutral atoms,” arXiv: 1506.04419 (2015).
 - ⁵¹ J. Rushton, M. Aldous, and M. Himsworth, “The feasibility of a fully miniaturized magneto-optical trap for portable ultracold quantum technology,” *Rev. Sci. Instrum.* **85**, 121501 (2014).
 - ⁵² T. Zhang and G.-B. Jo, “One-dimensional sawtooth and zigzag lattices for ultracold atoms,” arXiv:1510.02015 (2015).
 - ⁵³ S. Flach, D. Leykam, J. D. Bodyfelt, P. Matthies, and A. S. Desyatnikov, “Detangling flat bands into Fano lattices,” *EPL* **105**, 30001 (2014).
 - ⁵⁴ M. Metcalf, G.-W. Chern, M. Di Ventra, and C.-C. Chien, “Matter-wave propagation in optical lattices: geometrical and flat-band effects,” arXiv: 1502.04975 (2015).
 - ⁵⁵ S. Mukherjee and R. R. Thomson, “Observation of localized flat-band modes in a one-dimensional photonic rhombic lattice,” arXiv:1509.08445 (2015).
 - ⁵⁶ S. Taie, H. Ozawa, T. Ichinose, T. Nishio, S. Nakajima, and Y. Takahashi, “Matter-wave localization and delocalization of ultracold bosons in an optical Lieb lattice,” arXiv:1506.00587 (2015).
 - ⁵⁷ R. A. Vicencio, C. Cantillano, and L. Morales-Inostroza, “Observation of Localized States in Lieb Photonic Lattices,” *Phys. Rev. Lett.* **114**, 245503 (2015).
 - ⁵⁸ S. Mukherjee, A. Spracklen, D. Choudhury, N. Goldman, P. Öhberg, E. Andersson, and R. R. Thomson, “Observation of a Localized Flat-Band State in a Photonic Lieb Lattice,” *Phys. Rev. Lett.* **114**, 245504 (2015).
 - ⁵⁹ F. A. Mikailov, E. Şentürk, L. Tümbek, T. G. Mammadov, and T. S. Mammadov, “Thermal hysteresis and memory effects in TI-GaSe₂ crystal with incommensurate phase,” *Phase Transitions* **78**, 413–419 (2006).
 - ⁶⁰ A. M. Panich, “Electronic properties and phase transitions in low-dimensional semiconductors,” *J. Phys.: Condens. Matter* **20**, 293202 (2008).